DOI: 10.17617/2.3187774
Proceedings of the 9th Solar Polarization Workshop SPW9
A workshop held in Göttingen, Germany, from August 26 to August 30, 2019
Achim Gandorfer, Andreas Lagg, Kerstin Raab (eds.)

Magnetic Sensitivity in the Wings of the Linear Polarization Profiles of the Hydrogen Lyman-α Line

E. Alsina Ballester[1,*], L. Belluzzi[1,2], and J. Trujillo Bueno[3,4,5]

[1]Istituto Ricerche Solari Locarno, Locarno Monti, Switzerland
[2]Kiepenheuer-Institut für Sonnenphysik, Freiburg, Germany
[3]Instituto de Astrofísica de Canarias, La Laguna, Spain
[4]Departamento de Astrofísica, Universidad de La Laguna, La Laguna, Spain
[5]Consejo Superior de Investigaciones Científicas, Spain
[*]*Email:* ernest@irsol.ch, belluzzi@irsol.ch, jtb@iac.es

Abstract. The intensity and polarization profiles of the Lyman-α spectral line encode crucial information on the thermodynamic and magnetic structure of the upper layers of the solar atmosphere. In addition to providing high-quality spectropolarimetric data, the Chromospheric Lyman-Alpha Spectro-Polarimeter (CLASP) sounding rocket experiment produced interesting broadband images, both in intensity and linear polarization. Here, we present a theoretical investigation on the wavelength-integrated linear polarization signals emerging from models of the solar atmosphere in the presence of a magnetic field. We show that these signals are dominated by the scattering polarization in the wings, which are sensitive to the magnetic field through the magneto-optical effects. The validity of neglecting the influence of fine structure when modeling the wavelength-integrated scattering polarization signal of this line is also discussed. Finally, we show that a very good qualitative agreement with the broadband Q/I images obtained by the CLASP slit-jaw image can be reached with calculations that account for the joint action of scattering polarization with partial frequency redistribution and magneto-optical effects.

1 Introduction

In the chromosphere-corona transition region (TR), the temperature suddenly rises from $\sim 10^4$ K to $\sim 10^6$ K. During recent years, a number of physical explanations for this phenomenon have been proposed, highlighting the need for more detailed observational data on the thermal and magnetic properties of the TR and underlying layers. The hydrogen Lyman-α resonance line of the solar disk radiation, the strongest emission line in the solar ultraviolet spectrum, represents an especially valuable observational window in this regard. The near wing and line-center photons of this line encode information on the TR and upper chromosphere. Radiative transfer (RT) investigations of such line (Trujillo Bueno et al. 2011; Belluzzi et al. 2012; Štěpán et al. 2015) showed that scattering polarization signals provide crucial details on the thermal structure of such atmospheric regions – particularly in relation to the radiation anisotropy – and, within the Doppler core, they are sensitive to the pres-

ence of magnetic fields through the Hanle effect. Such theoretical predictions motivated the launch of the Chromospheric Lyman-Alpha Spectro-Polarimeter (CLASP) sounding rocket experiment, which observed the intensity and linear polarization of this line in relatively quiet regions of the Sun, with the slit oriented radially, spanning from off-limb positions towards disk center. The unprecedented spectropolarimetric data provided by CLASP (see Kano et al. 2017) permitted to constrain the degree of corrugation of the surface of the TR (Trujillo Bueno et al. 2018).

On the other hand, the photons of the hydrogen Lyman-α line outside the line-core region originate from significantly deeper atmospheric layers. For example, at 1 Å from line center, the height at which the optical depth is unity is a few hundred km below the TR. Because the Q/I and U/I signals produced by scattering processes at such wavelengths are insensitive to the Hanle effect, it was believed until recently that they are insensitive to the presence of magnetic fields, thus providing information only on the thermal structure of the atmospheric regions from where they emerge. However, recent investigations based on numerical RT calculations have revealed that the wing scattering polarization signals of strong chromospheric lines such as the Mg II h & k lines (Alsina Ballester et al. 2016; del Pino Alemán et al. 2016), the Sr II line at 4078 Å (Alsina Ballester et al. 2017), the Ca I line at 4227 Å (Alsina Ballester et al. 2018), and the H I Lyman-α line (Alsina Ballester et al. 2019) all present a clear magnetic sensitivity. For such resonance lines, the effects of partial frequency redistribution (PRD) in scattering processes give rise to large and broad Q/I signals. In the presence of a longitudinal magnetic field, such signals are modified by magneto-optical (MO) effects, in particular by those described by the ρ_V coefficient, which couples the transfer equations for Stokes Q and U, thereby inducing a rotation of the plane of linear polarization of the radiation propagating through the solar atmosphere (see Alsina Ballester et al. 2016) as well as an effective decrease of its polarization fraction (see Appendix of Alsina Ballester et al. 2018). In this work, we highlight the influence of such effects in the Q/I and U/I signals of Lyman α, even in the presence of comparatively weak magnetic fields.

In addition to the aforementioned spectropolarimetric observations, the CLASP slit-jaw system obtained broadband images of the solar disk over a larger field of view (FOV), containing a bright plage region and a multitude of network features. Serendipitously, such measurements were not only taken in intensity but also in Q/I. Therein, strongly depolarized features are apparent, which roughly correspond to the regions with higher magnetic activity. In the present publication we attempt to mimic such results using the synthetic wavelength-integrated signals obtained from RT calculations, accounting for PRD effects and the impact of magnetic fields through the Hanle and Paschen-Back effects.

In Section 2 we discuss the assumptions we have made for carrying out such RT investigations, as well the numerical scheme we have used and the geometry of the problem. In Section 3 we present the results of such investigations, including a comparison between modeling the Lyman-α line with a two-term and a two-level spinless atomic model. In this section, we evaluate the sensitivity of the Q/I and U/I wings to MO effects and the importance of the contribution from the line core to the wavelength-integrated Q/I signal. We also present the two-dimensional images obtained with the aforementioned synthetic profiles, replicating the intensity and Q/I broadband images obtained by CLASP. The conclusions of this work are presented in Section 4.

2 Formulation of the problem

The H I Lyman-α line originates from the transition between the hydrogen energy levels with principal quantum numbers $n = 1$ and $n = 2$. The intensity and scattering polarization profiles of this line can suitably be modeled considering a two-term atom, taking into account the contributions from the transitions between the $^2\mathrm{P}_{1/2}$ and $^2\mathrm{P}_{3/2}$ fine structure (FS) levels of the upper term and the $^2\mathrm{S}_{1/2}$ level of the lower term, as well as the quantum interference between the upper levels (e.g., Belluzzi et al. 2012).

The synthetic profiles presented hereafter have been calculated using a numerical scheme analogous to that described in Alsina Ballester et al. (2017) for a two-level atom with an unpolarized lower level, generalized here for more complex atomic models. The version of the polarized radiative transfer (RT) code used in this work is capable of treating the generation and transfer of polarized radiation for a two-term atom with an unpolarized lower term, accounting for the scattering of polarized, anisotropic radiation (i.e., scattering polarization). It also takes into account its modification due to the presence of a magnetic field due to both the Hanle effect and the incomplete Paschen-Back effect. Although the code also allows for the inclusion of hyperfine structure in the atomic model, it is not required to treat the problem discussed here and will be omitted hereafter.

The non-LTE RT problem considered here requires the solution of two coupled sets of equations. One one hand, the Stokes vector $\mathbf{I}(\nu, \mathbf{\Omega})$ for the radiation propagating through the atmospheric material, with direction $\mathbf{\Omega}$ and frequency ν, is characterized by the RT equation

$$\frac{\mathrm{d}}{\mathrm{d}s}\mathbf{I} = \boldsymbol{\varepsilon} - \mathbf{K}\,\mathbf{I}\,. \tag{1}$$

All the quantities appearing in this expression have dependencies on ν and $\mathbf{\Omega}$ which, for notational simplicity, are not given explicitly. The spatial coordinate along the ray path is written as s, the four Stokes components of the emissivity are given by $\boldsymbol{\varepsilon}$, and the so-called propagation matrix is a 4×4 matrix of the form

$$\mathbf{K} = \begin{pmatrix} \eta_I & \eta_Q & \eta_U & \eta_V \\ \eta_Q & \eta_I & \rho_V & -\rho_U \\ \eta_U & -\rho_V & \eta_I & \rho_Q \\ \eta_V & \rho_U & -\rho_Q & \eta_I \end{pmatrix}. \tag{2}$$

The diagonal element η_I is the absorption coefficient for intensity, whereas the elements η_X with $X = Q, U, V$ describe the differential absorption of the corresponding Stokes parameter (dichroism) and the anomalous dispersion coefficients ρ_X characterize couplings between the Stokes components other than I. The expressions for their continuum contributions can be found in Alsina Ballester et al. (2017); those for their line contributions can be found as described in Chapter 7 of Landi Degl'Innocenti & Landolfi (2004) for a two-term atomic model with an unpolarized lower term.

Assuming that the lower term (i.e., the level $^2\mathrm{S}_{1/2}$) is unpolarized and infinitely sharp (such assumptions are perfectly suitable considering that this is the ground level for hydrogen) and neglecting stimulated emission, there exists a closed analytical solution for the statistical equilibrium equations. In this case, the line scattering contribution to the emission coefficient can be directly related to the incident radiation field using the redistribution matrix formalism

(Stenflo 1994; Hummer 1962)

$$\varepsilon_i^{\ell,\mathrm{sc}}(\nu,\mathbf{\Omega}) = k_M \int \mathrm{d}\nu' \oint \frac{\mathrm{d}\mathbf{\Omega}'}{4\pi} \sum_{j=0}^{3} \mathcal{R}(\nu',\mathbf{\Omega}',\nu,\mathbf{\Omega})_{ij}\, I_j(\nu',\mathbf{\Omega}')\,, \tag{3}$$

where the labels i and j can take values 0, 1, 2, and 3 corresponding to the Stokes parameters I, Q, U, and V, respectively. $I_j(\nu',\mathbf{\Omega}')$ is the $j-$th Stokes component for incident radiation with frequency ν' propagating in direction $\mathbf{\Omega}'$. Throughout this work, we have used the expressions for the redistribution matrix given in the Appendix of Bommier (2017) (for errata, see also Bommier 2018), suitably transformed into the observer's reference frame in analogy to the discussion presented in Alsina Ballester et al. (2017). For the term of the redistribution matrix that quantifies coherent scattering processes, we have made use of the angle-averaged approximation (Rees & Saliba 1982). Concerning the collisional rates appearing in the branching ratios and in the damping parameter in the absorption and emission profiles, those for elastic collisions have been calculated considering a Van der Waals broadening contribution following Chapter 7 of Landi Degl'Innocenti & Landolfi (2004) and a Stark broadening contribution following Sutton (1978). Those for the inelastic collisional rates have obtained following Przybilla & Butler (2004). Furthermore, we have used the expression for the thermal contribution to the line emissivity given in Belluzzi et al. (2013). The continuum contribution to the emissivity is given in Alsina Ballester et al. (2017). The quantity k_M appearing in Equation (3) – as well as in the expressions for the coefficients of the propagation matrix – is the frequency-integrated absorption coefficient, which depends on the number density of atoms in the lower level, $\mathcal{N}_\ell$. The value for $\mathcal{N}_\ell$ at each height grid point in the considered atmospheric model has been taken from a converged solution of the non-LTE RT problem for intensity only, obtained with the RH code of Uitenbroek (2001).

Because the RT equation and the expressions for the line scattering contribution to the emissivity shown in Equation (3) are coupled, it is customary to treat such problems through iterative methods (e.g. Olson et al. 1986; Trujillo Bueno & Fabiani Bendicho 1995; Trujillo Bueno & Manso Sainz 1999), solving the two sets of equations iteratively until a self-consistent solution is reached. The accelerated lambda iteration scheme we have implemented is formally identical to the one presented in Alsina Ballester et al. (2017), albeit considering a redistribution matrix that is suitable for a two-term atomic model.

The results of the non-LTE RT calculations presented in the following sections have been obtained considering one-dimensional static solar atmospheric models. In particular, we have used the semiempirical models of Fontenla et al. (1993); hereafter FAL models. The line of sight (LOS) for the emergent radiation is specified only by $\mu = \cos\theta$, in which θ is the heliocentric angle (here, this is equivalent to the inclination with respect to the local vertical). The initial guess for the radiation field was taken from a converged solution of the RT problem for intensity only, obtained with RH. Such radiation field is axially symmetric with respect to the local vertical. Indeed, for the problems considered here, cylindrical symmetry may be broken only by the presence of a magnetic field. Henceforth, we consider deterministic magnetic fields whose strengths and orientations are the same at all atmospheric heights. Their orientations are specified by the inclination θ_B with respect to the local vertical and the azimuth χ_B, relative to the plane defined by the local vertical and the LOS. This geometry is illustrated in Figure 1 of Alsina Ballester et al. (2018). Except where otherwise noted, throughout this work the positive direction for Stokes Q is taken parallel to the nearest limb.

3 Results

3.1 The influence of fine structure on the wing scattering polarization

Observing that the FS levels of the upper term are very close to each other in comparison with the Einstein coefficient for spontaneous emission ($A_{u\ell} = 6.26 \cdot 10^8$ s^{-1} for both considered transitions), it can be shown that, far from line center, this line behaves in resonance scattering as a spinless two-level 0 − 1 transition. This is in compliance with the principle of spectroscopic stability; the results of any physical experiment for which the FS is unimportant may be characterized both through a description that accounts for spin and through a simplified description that disregards it. Indeed, the left panel of Figure 1 shows a compari-

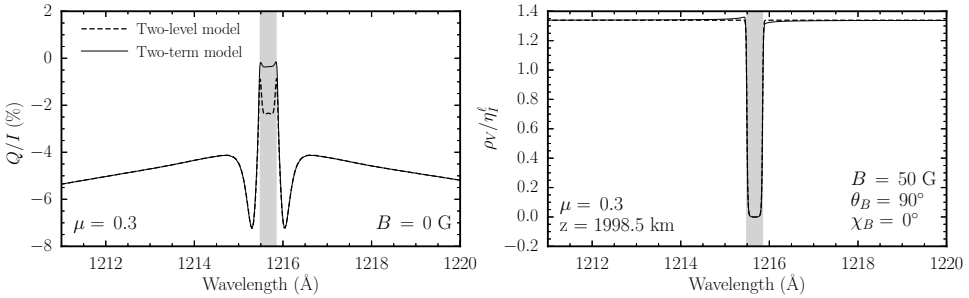

Figure 1. Left panel: Q/I scattering polarization profiles of the H I Lyman-α line, obtained with the RT code described in the text. Such calculations have been made in the absence of a magnetic field and considering the FAL-C atmospheric model for a LOS with $\mu = 0.3$. The synthesized profiles obtained accounting for FS in the atomic model (solid curve) and neglecting it (dashed curve) are compared. Right panel: Ratio of ρ_V over the line absorption coefficient η_I^ℓ for $\mu = 0.3$, obtained considering the same two atomic models in the presence of a 50 G magnetic field. We have taken such field with an inclination $\theta_B = 90°$ (i.e., horizontal) and azimuth $\chi_B = 0°$, which maximizes its longitudinal component. We have taken the Doppler broadening and collisional rates corresponding to a height of 1998.5 km in the FAL-C atmospheric model. The shaded gray area shown in both panels indicates the spectral region where the two-level approximation is not valid.

son of the scattering polarization profiles obtained from both descriptions, resulting from the RT calculations described above. They have been carried out in the absence of a magnetic field and considering the FAL-C semiempirical atmospheric model. Whereas a considerable FS depolarization in Q/I is found in the line core, the results obtained with a two-level spinless atomic model and with a two-term atomic model present an excellent agreement outside the spectral region of up to 180 mÅ from line center, shaded in gray in the figure. Hereafter, we refer to this region as the line-core region. A similar agreement between the two modeling approaches can be found for the ratio of ρ_V over the line absorption coefficient for intensity η_I^ℓ outside of the core region. This can be seen in the right panel of Figure 1 in the presence of a 50 G horizontal magnetic field, selecting the azimuth so that the longitudinal component is maximal ($\chi_B = 0°$). Such ratios have been calculated taking the parameters corresponding to a height of 1998.5 km in the FAL-C atmospheric model. Observing that ρ_V is the only off-diagonal element of the propagation matrix whose ratio over η_I^ℓ differs significantly from zero outside the Doppler core (see Alsina Ballester et al. 2016) and that,

for magnetic fields of strengths typically found in the solar atmosphere, the emission coefficient in the line wings is insensitive to the presence of a magnetic field in any of its Stokes components (e.g., Section 10.4 of Landi Degl'Innocenti & Landolfi (2004)), it is apparent that the magnetic sensitivity in the wings is controlled by the ρ_V/η_I ratio, in which the continuum contribution to the absorption coefficient is also accounted for. Thus, we conclude that both the wing scattering polarization of H I Lyman α and its magnetic sensitivity can be well modeled outside of the line-core spectral region considering a two-level spinless atom. Furthermore, it can be shown (see Appendix of Alsina Ballester et al. 2019) that in the absence of collisions $\rho_V/\eta_I^\ell = 4\pi\nu_L \cos\alpha_B/A_{u\ell}$, where ν_L is the Larmor frequency and α_B is the angle between the magnetic field and the LOS. Interestingly, the Hanle critical field, i.e., the field strength that characterizes the onset for the Hanle effect, also scales with the $\nu_L/A_{u\ell}$ ratio, indicating that both effects should be expected to have an impact at a similar range of field strengths.

3.2 The influence of magneto-optical effects on the wing scattering polarization

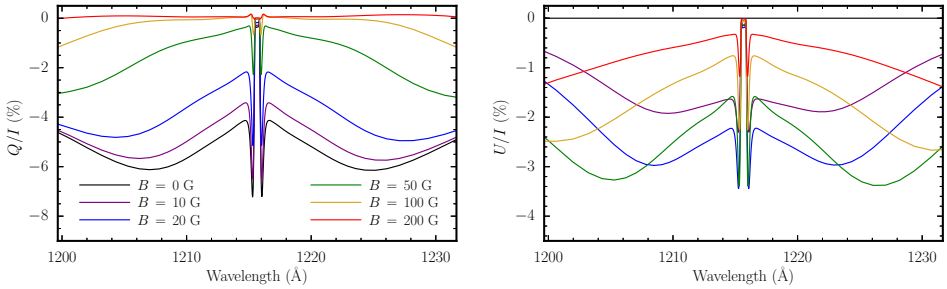

Figure 2. Stokes Q/I (left panel) and U/I (right panel) scattering polarization profiles, calculated for the FAL-C atmospheric model for a LOS with $\mu = 0.3$. Deterministic magnetic fields with inclination $\theta_B = 90°$, azimuth $\chi_B = 0°$, and constant strength at all atmospheric grid points are considered. The various colored curves represent different field strengths (see legend). A two-term atomic model has been used for all calculations.

Figure 2 shows the linear polarization profiles resulting from RT calculations in the FAL-C atmospheric model, considering a two-term atom, in the presence of horizontal magnetic fields with a large longitudinal component, for various field strengths. As in the previous figure, a LOS with $\mu = 0.3$ has been considered. As expected, the Hanle effect operates in the line core, causing a depolarization and rotation of the plane of linear polarization, giving rise to a U/I signal. For this particular geometry, the magneto-optical effects quantified by ρ_V have a qualitatively similar impact, causing a decrease in the amplitude of the Q/I signal and the appearance of a magnetically-sensitive U/I signal. We have checked that, by performing the same calculations but artificially setting ρ_V to zero for all magnetic field strengths, no appreciable magnetic sensitivity is found in the Q/I and U/I wings. Stronger magnetic fields are required to appreciably modify the scattering polarization signals farther from the line core, because the ρ_V/η_I ratio decreases due to the larger relative contribution of the continuum absorption coefficient. It is worth noting that MO effects give rise to a

substantial modification of the wing linear polarization signals for field strengths of 10 G – well below the Hanle critical field for the Lyman-α line, of about 53 G.

3.3 Frequency-integrated Stokes profiles

In addition to spectropolarimetric data, the CLASP mission provided, through its slit-jaw system, broadband images over a large field of view (FOV). Such images were not only taken in intensity, in which a bright plage region and a multitude of network features were appreciable, but also in Q/I (see Figure 1A of Kano et al. 2017). The reference direction for Stokes $Q > 0$ was taken perpendicular to the slit. Large negative signals can be found throughout the FOV, whose amplitude increases at positions closer to the limb. In addition, a decrease in amplitude of these signals is found in regions roughly corresponding to the plage and network regions observed in the intensity image.

In order to evaluate the impact of PRD and MO effects on the Q/I signals and compare them to the above-mentioned broadband observations, we have integrated the calculated Stokes profiles over wavelength. In order to suitably mimic the observations obtained with the slit-jaw system, whose broadband filter has a full width at half maximum (FWHM) of 70 Å, the spectral integration has been carried out by weighting the Stokes profiles with a Gaussian function centered around the baricenter of the Lyman-α line. The resulting center-

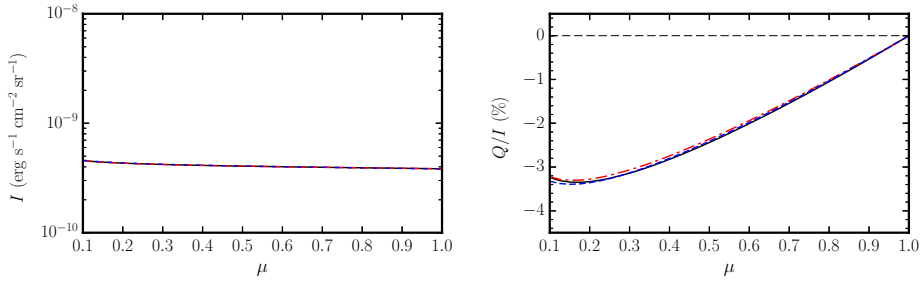

Figure 3. CLV of the spectrally-integrated intensity (left panel) and Q/I (right panel) signals, calculated in the absence of a magnetic field and considering the FAL-C atmospheric model. The profiles obtained accounting for FS and the contribution to Q/I from the core region (black solid curves), accounting for FS but neglecting the contribution to Q/I from the core region (red dashed-dotted curves), and neglecting both FS and the contribution to Q/I from the core region (blue dashed curves) are compared. The direction for positive Stokes Q is taken parallel to the limb. The thin black dashed line in the right panel corresponds to $Q/I = 0$.

to-limb variations (CLV) of the wavelength-integrated intensity and Q/I signals, calculated in the absence of a magnetic field, are shown in Figure 3. The results obtained for a two-term atomic model (i.e., accounting for FS), both (a) accounting for the contribution to Q from the line-core region (the shaded region shown in Figure 1) in the spectral integration and (b) neglecting it by setting $Q = 0$ within such region, and (c) considering a two-level spinless atomic model, also neglecting the line-core contribution to Stokes Q, are compared. Note that the spectrally-integrated Q/I signal changes very little whether the contribution from the line core is accounted for or not, implying that the dominant contribution is from

outside such spectral region. This can be explained because, although Lyman-α presents a large emission peak in intensity, the Gaussian weighting function has a large variance and because the Q/I signals have a small amplitude in the line core, relative to those farther into the wings (see left panel of Figure 1). The wavelength-integrated Q/I signal obtained when neglecting FS and the contribution from the line-core region presents an excellent agreement with the calculations accounting for FS, consistent with the discussion in Section 3.1. Having demonstrated the validity of such approximation, the results shown hereafter have been obtained neglecting both FS in the atomic model and the contribution from the line core to Stokes Q, in the interest of reducing the computational cost.

A slight limb-brightening is found in the wavelength-integrated intensity signal, in qualitative agreement with the observations reported by Warren et al. (1998). However, this contrasts with the findings of Roussel-Dupre (1982) and Curdt et al. (2008), in which little or no CLV was found. Such apparent disagreement may be attributed to the fact that the spectrally-integrated profiles of the present work take into account contributions from much farther into the wings. Indeed, we have checked that, by performing the integration over a narrower spectral range (e.g., up to 10 Å from line center), the aforementioned CLV is no longer appreciable.

In order to reproduce the two-dimensional CLASP slit-jaw image we have divided it into four distinct regions, according to the $\log I$ value of the considered pixel on the image, relative to the average value, taken excluding the pixels corresponding to off-limb positions. Region A contains the pixels whose $\log I$ value is larger than 2.15 times the average and are in the lower left quadrant, corresponding to the plage region. Regions B and C contain the pixels that do not meet the former conditions but whose $\log I$ values are, respectively, larger than 1.48 times the average value and between 0.81 and 1.48 times the average value. Such regions correspond to inner and outer network regions, respectively. The rest of the pixels belong to region D, corresponding to the internetwork regions. For each of these regions, we have carried out RT calculations considering different atmospheric models and magnetic field inclinations and strengths. The synthesized profiles pertaining to the plage region A have been calculated in the FAL-P atmospheric model and a vertical magnetic field of 450 G has been used. For the inner network region B the FAL-F model has been used, taking a vertical field of 150 G. Concerning regions C and D, the FAL-C atmospheric model has been considered. For the outer network region C, we have imposed a vertical magnetic field of 50 G. For the internetwork region D, in order to mimic the case of a horizontal field with an azimuth that changes over scales smaller than the resolution element of the instrument, but larger or comparable to the mean free path of the line's photons, we have averaged over the results of twelve different calculations, each of them with a 10 G horizontal field and changing the azimuth by steps of 30° (i.e., we have performed a so-called macro-turbulent average). For all four regions, the calculations have also been performed in the absence of magnetic field.

The resulting I and Q/I, considering such models, are displayed as a function of μ in Figure 4, both accounting for the aforementioned magnetic fields and neglecting them. As expected, the intensity signal strongly depends on the choice of atmospheric model, because the thermodynamical parameters of the various FAL models were obtained from regions of the solar atmosphere with different levels of activity. As for the CLV for Q/I, we observe that in the absence of a magnetic field the well-known $1-\mu^2$ trend for scattering polarization is followed, independent of the choice of atmospheric model. However, in the presence of

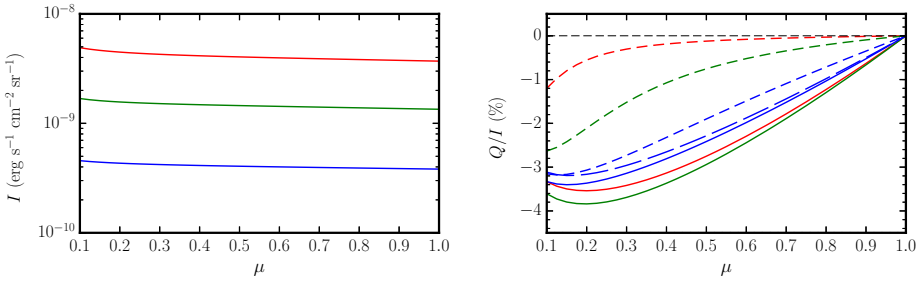

Figure 4. CLV of the spectrally-integrated intensity (left panel) and Q/I (right panel) profiles for the various regions introduced in the text. All solid curves represent calculations carried out in the absence of a magnetic field. Red curves represent the results of calculations considering the FAL-P atmospheric model, with the dashed curve representing the calculation in the presence of a 450 G vertical field. Green curves represent calculations using FAL-F, with the dashed curve representing the calculation in the presence of a 150 G vertical field. Blue curves correspond to calculations using the FAL-C model; the short dashed curve represents the results obtained in the presence of a 50 G vertical magnetic field and the long dashed curve represents the results obtained by performing an average over various calculations in the presence of 10 G horizontal fields with different azimuths. The reference direction for positive Stokes Q is taken parallel to the nearest limb. The thin black dashed line in the right panel corresponds to $Q/I = 0$. All the calculations have been carried out considering a two-level spinless atomic model and setting $Q = 0$ in the core region.

magnetic fields, such CLV are modified due to the impact of MO effects. In the presence of vertical magnetic fields, a strong depolarization is observed, not only for large μ-values but also closer to the limb, both because the longitudinal component of the magnetic field – although smaller – is still significant and because the radiation field illuminating the atoms is also modified by MO effects, thereby reducing the polarization of the outgoing radiation in scattering processes (e.g., Alsina Ballester et al. 2018). Indeed, in the presence of a 450 G vertical field the signal is almost completely depolarized, except at small μ-values. On the other hand, in the presence of horizontal 10 G magnetic fields, barely any depolarization is observed at large μ values, but closer to the limb the degree of depolarization is comparable to that of a 50 G vertical magnetic field.

In order to recreate the slit-jaw images from Figure 1A of Kano et al. (2017) using the spectrally-integrated synthesized profiles discussed above, we first determine for each pixel the corresponding $\mu = \cos\theta$, with θ the inclination of the LOS with respect to the local vertical (or radial direction), following

$$\mu = \sqrt{1 - \left(\frac{d}{R}\right)^2}, \tag{4}$$

where $R = 980$ arcsec is the solar disk radius and d is the distance in arcsec to the disk center, at coordinates $(x, y) = (10, -795)$. The intensity and Q/I images obtained using such data sets are shown in Figure 5, both in the absence of magnetic field and considering the

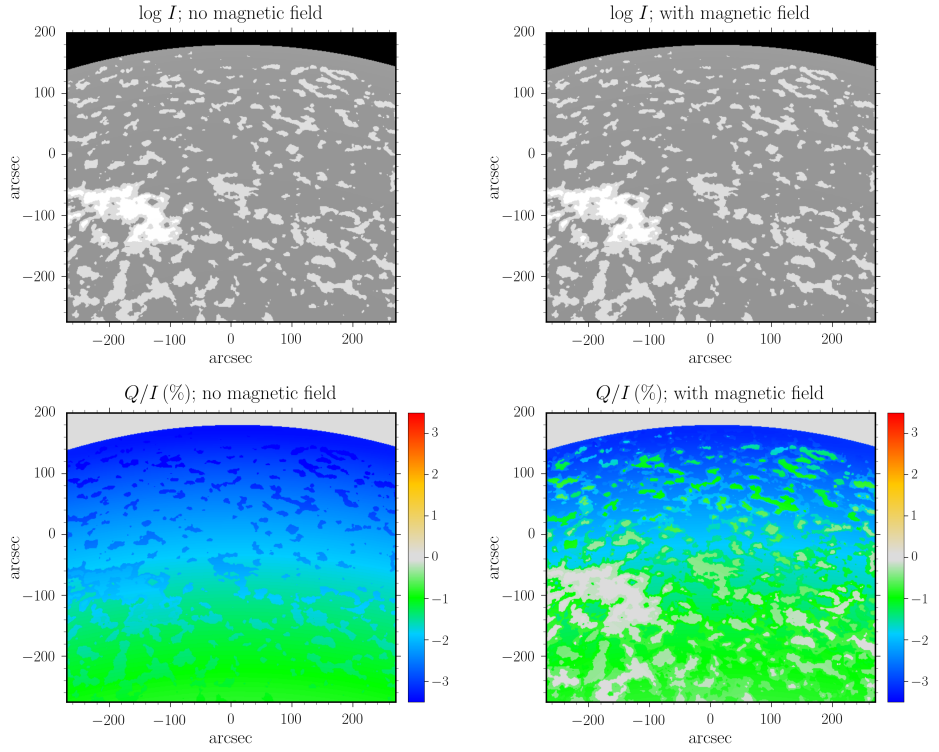

Figure 5. Modeling of the two-dimensional broadband images obtained by the CLASP slit-jaw system, using the synthetic profiles discussed in the text. The top panels show the spectrally-integrated log I signals, and the bottom panels show the ratio of the spectrally-integrated Q and I signals. The images in the left panels are obtained from calculations in the absence of a magnetic field, whereas those in the right panels are obtained from calculations taking into account the magnetic field configurations described in the text. The direction for positive Stokes Q is taken parallel to the X-axis.

magnetic field configurations discussed above. For the Stokes I image, a larger intensity is found in the regions corresponding to the plage and inner network structures. As expected, no appreciable change can be observed when accounting for the magnetic field. For the Q/I images the reference direction for positive Stokes Q has been taken parallel to the X-axis rather than parallel to the nearest limb at each individual pixel. Negative signals are found at all positions, with large overall amplitudes that increase as one approaches the limb. In the absence of magnetic fields, only minor changes in the Q/I amplitude can be observed depending on the atmospheric model considered in the calculation. When magnetic fields are taken into account, by contrast, the signals in the region corresponding to the plage are almost completely depolarized; significant depolarizations of the signals is also found in the inner network regions and, to a lesser extent, in the outer network regions. However the signals corresponding to the internetwork regions experience only a very modest decrease in

their Q/I amplitude. Thus, when the aforementioned magnetic fields are taken into account, the Q/I image presents a very good qualitative agreement with the one obtained by the CLASP slit-jaw system.

We point out that, by considering a larger number of one-dimensional atmospheric models whose thermodynamic parameters (including the magnetic field) represent common realizations of the solar atmosphere, it would be possible to replicate the broadband intensity and Q/I images discussed above to a higher degree of accuracy, still accounting only for the polarization produced by scattering processes and its modification due to the MO effects that operate in the wings. Nevertheless, it is worth noting that other physical mechanisms that cannot be taken into account in the present approach, such as symmetry-breaking effects due to horizontal inhomogeneities in the thermodynamical properties of the solar atmosphere, may strongly influence the resulting polarization signals. This represents a further motivation for the development of RT codes for polarized radiation that can consider three-dimensional atmospheric models, in addition to the magnetic field – including Hanle and Paschen-Back effects – and PRD effects in scattering.

4 Conclusions

A few years ago, it was theoretically discovered that the scattering polarization signals in the wings of many strong resonance lines are sensitive to the presence of magnetic fields via the MO effects that couple the transfer equations for Stokes Q and U (Alsina Ballester et al. 2017). The H I Lyman-α emission line presents particularly broad and large-amplitude scattering polarization wing signals, because of the strong influence of PRD phenomena in scattering processes. This has motivated RT investigations in order to evaluate the influence of MO effects for this line. A considerable sensitivity of the wing scattering polarization to longitudinal magnetic fields via such effects is found, even for fields considerably weaker than the Hanle critical field. Having treated this line both as a two-term atom and a two-level spinless atom (i.e., neglecting FS), we find that both modeling approaches yield an excellent agreement outside the line-core region, in compliance with the principle of spectroscopic stability.

The two-dimensional broadband images taken by CLASP show a multitude of depolarized features with an apparent correlation with the spatial regions having high activity. In order to mimic the observations with the broadband filter, we have integrated the synthetic profiles obtained from our RT calculations over wavelength, considering a Gaussian weighting function with a FWHM of 70 Å. Only small differences are found between the spectrally-integrated Q/I signals obtained taking into account the contribution from the line-core region and neglecting it, implying that the dominant contribution comes from the line wings. By carrying out RT calculations in which we consider magnetic field configurations typical of plage, network, and internetwork regions, accounting for the influence of MO effects, we are able to construct intensity and Q/I images that present a good qualitative agreement with the aforementioned observations.

Future developments in this investigation involve replicating the observed broadband images with a larger selection of data sets, in order to better reflect the complexity of the solar atmosphere. It would also be of interest to confront synthetic spectrally-integrated profiles with observed U/I images, in addition to those for intensity and Q/I. Finally, we emphasize

that an accurate RT modeling of the scattering polarization of this line requires accounting for the three-dimensional structure of the solar atmosphere, in addition to the joint action of scattering processes with PRD and the Hanle and Paschen-Back effects considered here.

Acknowledgements. E.A.B. and L.B. gratefully acknowledge financial support by the Swiss National Science Foundation (SNSF) through Grant 200021_175997. J.T.B. acknowledges the funding received from the European Research Council (ERC) under the European Union's Horizon 2020 research and innovation programme (ERC Advanced Grant agreement No. 742265). L.B. and J.T.B. acknowledge financial support through the Sinergia programme of the SNSF (Grant No. CRSII5_180238).

References

Alsina Ballester, E., Belluzzi, L., & Trujillo Bueno, J. 2016, ApJ, 831, L15
Alsina Ballester, E., Belluzzi, L., & Trujillo Bueno, J. 2017, ApJ, 836, 6
Alsina Ballester, E., Belluzzi, L., & Trujillo Bueno, J. 2018, ApJ, 854, 150
Alsina Ballester, E., Belluzzi, L., & Trujillo Bueno, J. 2019, ApJ, 880, 85
Belluzzi, L., Trujillo Bueno, J., & Štěpán, J. 2012, ApJ, 755, L2
Belluzzi, L., Landi Degl'Innocenti, E., & Trujillo Bueno, J. 2013, A & A, 551, A84
Bommier, V. 2017, A & A, 607, A50
Bommier, V. 2018, A & A, 619, C1
Curdt, W., Tian, H., Teriaca, L., et al. 2008, A & A, 492, L9
del Pino Alemán, T., Casini, R., & Manso Sainz, R. 2016, ApJ, 830, L24
Fontenla, J. M., Avrett, E. H., & Loeser, R. 1993, ApJ, 406, 319
Hummer, D. G. 1962, MNRAS, 125, 21
Kano, R., Trujillo Bueno, J., Winebarger, A., et al. 2017, ApJ, 839, L10
Landi Degl'Innocenti, E., & Landolfi, M. 2004, Polarization in Spectral Lines (Dordrecht: Kluwer Academic Publishers)
Olson, G. L., Auer, L. H. & Buchler, J. R. 1986, J. Quant. Spectrosc. Radiat. Transfer, 35, 431
Przybilla, N., & Butler, K. 2004, ApJ, 609, 1181
Rees, D. E. & Saliba, G. J. 1982, A & A, 115, 1
Roussel-Dupre, D. 1982, ApJ, 256, 284
Scharmer, G. B. 1981, ApJ, 249, 720
Sutton, K. 1978, J. Quant. Spectrosc. Radiat. Transfer, 20, 333
Štěpán, J., Trujillo Bueno, J., Leenaarts, J., & Carlsson, M. 2015, ApJ, 803, 65
Stenflo, J. 1994, Solar Magnetic Fields. Polarized Radiation Diagnostics (Dordrecht: Kluwer Academic Publishers)
Trujillo Bueno, J., Štěpán, J., & Casini, R. 2011, ApJ, 738, L11
Trujillo Bueno, J. & Fabiani Bendicho, P. 1995, ApJ, 455, 646
Trujillo Bueno, J. & Manso Sainz, R. 1999, ApJ, 516, 436
Trujillo Bueno, J., Štěpán, J., Belluzzi, L., et al. 2018, ApJ, 866, L15
Uitenbroek, H. 2001, ApJ, 557, 389
Warren, H. P., Mariska, J. T., & Wilhelm, K. 1998, ApJS, 119, 105